

# A level-set method for imaging salt structures using gravity data

Wenbin Li<sup>1</sup> and Wangtao Lu<sup>2</sup> and Jianliang Qian<sup>3</sup>

<sup>1</sup> Department of Mathematics, Michigan State University, East Lansing, MI 48824. Email:  
[wenbinli@math.msu.edu](mailto:wenbinli@math.msu.edu)

<sup>2</sup> Department of Mathematics, Michigan State University, East Lansing, MI 48824. Email:  
[wangtaol@math.msu.edu](mailto:wangtaol@math.msu.edu)

<sup>3</sup> Department of Mathematics, Michigan State University, East Lansing, MI 48824. Email:  
[qian@math.msu.edu](mailto:qian@math.msu.edu)

(November 3, 2015)

Running head: **Level-set inversion of gravity data**

## ABSTRACT

We present a level-set method for the inverse gravimetry problem of imaging salt structures with density contrast reversal. Under such a circumstance, a part of the salt structure contributes two completely opposite anomalies that counteract with each other, making itself unobservable to the gravity data. As a consequence, this amplifies inherent non-uniqueness of the inverse gravimetry problem so that it is much more challenging to recover the whole salt structure from the gravity data. To alleviate the severe non-uniqueness, it is reasonable to assume that density contrast between the salt structure and the surrounding sedimentary host depends upon the depth only and is known a priori. Consequently, the original inverse gravity problem reduces to a domain inverse problem, where the supporting domain of the salt body becomes the only unknown. We use a level-set function to parametrize the boundary of the salt body so that we reformulate the domain inverse problem into a nonlinear optimization problem for the level-set function, which is further solved for by a gradient descent method. Both 2-D and 3-D experiments on the SEG/EAGE salt model are carried out to demonstrate the effectiveness and efficiency of the new method. The

algorithm is able to recover dipping flanks of the salt model, and it only takes 40 minutes in a 2.5 GHz CPU to invert for a 3-D model of 97,000 unknowns.

## INTRODUCTION

As a ductile material which is impermeable to hydrocarbons, salt serves as an effective agent for trapping oil and gas in nature (Farmer et al., 1996). Currently, the salt basins worldwide have been one of the places to find the most prospective hydrocarbon reservoirs (Leveille et al., 2011), so that the oil industry's interest is growing in the exploration of salt-related structures. While the overwhelming number of seismic imaging techniques are currently acoustic in nature, seismic methods have encountered many difficulties in the interpretation of complex salt geometries (Bain et al., 1991; Leveille et al., 2011). Therefore non-seismic tools are needed to produce better representations for salt structures of poor illumination, and the gravity inversion is one of these tools available to us.

Salt is a material with a different density compared to its surrounding sediments so that the resulting density contrast generates anomalous acceleration in the gravity data. A gravity inversion method can be utilized to find out the density contrast which gives information of the shape and location of a salt body. In particular, salt is relatively incompressible and retains a low density even after burial. However, the surrounding sediments are compact and have densities which increase with respect to depth. Depending on the depth of a salt body, three scenarios can occur in the density contrast between the salt body and the sedimentary background: positive density contrast, negative density contrast, and nil zone (Jorgensen and Kisabeth, 2000; Routh et al., 2001; Krahenbuhl and Li, 2006; Hatch and Annecchione, 2010). In the shallow region the salt body is of greater density than its sedimentary host, and this leads to a positive density contrast which generates a positive gravity anomaly in the measured gravity data. While the salt body extends to a large depth its density becomes smaller than those of the surrounding sediments, and this leads to a negative density contrast, inducing negative gravity anomaly in the measured gravity data. Moreover, there exists a depth interval over which the salt density is within the range of sediment densities; such a depth region has been termed as the nil zone (Bain et al., 1993) in that the salt/sediment density contrast is nil.

The complex scenarios involving nil zone and density-contrast reversal can cause major difficulties in the gravity inversion of salt structures. The portion of a salt body within the nil zone does not contribute to anomaly in the gravity data, so that the gravity method essentially has no information of this portion of salt (Bain et al., 1991). Moreover, density-contrast reversal in the underlying structure leads to the effect of annihilator (Gibson and Millegan, 1998) so that the deep portion of the salt body with negative density contrast generates negative anomaly in the gravity data which cancels out the positive anomaly generated by the shallow portion with positive density contrast. The presence of nil zone and the effect of annihilator increase ill-posedness of the gravity inversion in salt imaging. To overcome these difficulties, a natural consideration is to incorporate a prior geological information into the inversion to help alleviate non-uniqueness of the inversion and ensure that the inverted solution conforms to a realistic earth model.

According to Krahenbuhl and Li (2006), existing methods for salt imaging using gravity data fall under two general categories: the first is interface inversion and the second is generalized density inversion. Assuming a simple profile for the salt body and a known density contrast, interface-inversion methods look for the shape of the salt-sediment interface (Barbosa et al., 1999; Cheng et al., 2003; Krahenbuhl and Li, 2006; Silva Dias et al., 2011; Ennen and Hall, 2011; Barnes and Barraud, 2012; Cai and Zhdanov, 2015); additional geological information is usually incorporated into the inversion process. For example, in Cheng et al. (2003) the interface inversion requires the knowledge of both the top of a salt body and a part of the base of the salt body so as to determine the complete base of the salt body. A drawback of this type of interface inversion is the assumed simple geometry which hinders its application to imaging complicated salt structures. On the other hand, direct density-inversion methods make almost no explicit assumptions on the geometry of a salt body. The targeted region is divided into a large number of cells with fixed sizes and unknown constant densities, and those in-cell densities are determined by the inversion (Li and Oldenburg, 1998). In particular, the in-cell densities are found to fit the observed data by minimizing an objective function, and Tikhonov regularization and depth weighting are also introduced into the objective function to ensure that the solution is geologically reasonable. To

further handle the complex scenarios in salt imaging, additional geological information is usually incorporated into inversion algorithms (Oldenburg et al., 1998; Li, 2001), such as imposing lower and upper bounds on the density contrast. For example, in Li (2001) the inversion algorithm allows different density bounds for different individual cells; one can freeze the density contrast value and enforce exact salt structure in certain regions (such as the top of the salt body) by applying a very tight pair of density bounds.

In Krahenbuhl and Li (2006) the authors have combined merits of the above two categories of methods and proposed a binary inversion algorithm for salt imaging. The density contrast is characterized by a binary variable, which equals either zero or one, where one represents the value expected at a given depth; the characteristic variable is inverted to recover the shape of a salt body. This binary formulation enables us to explicitly incorporate density contrast values into the density inversion. The difficulty, however, is that the binary nature of the inversion variable requires a derivative-free optimization algorithm, which is usually of demanding computational cost. Krahenbuhl and Li (2006) have adopted the genetic algorithm to solve the gravity inverse problem with binary constraints, and the resulting algorithm has been applied to only 2.5-D gravity inverse problems.

In this paper, starting from the idea of binary formulation for the density contrast as proposed in Krahenbuhl and Li (2006) which is capable of handling the problem of nil zone and the effect of annihilator in salt imaging, we apply the level-set method (Osher and Sethian, 1988) to manipulate the binary structure in a continuous framework. In contrast to working on a binary variable directly, we use the level-set function along with the Heaviside function to represent the binary density contrast in salt imaging. The level-set function is maintained to be a continuous signed-distance function to the salt-sediment interface, and this continuous function is sought after to recover the binary salt structure. The advantage of the proposed level-set algorithm is that we can reconstruct the binary structure using a derivative-based optimization method. The proposed algorithm can be carried out efficiently to invert for the 3-D SEG/EAGE salt model (Aminzadeh, 1996) on a personal computer.

The level-set method (Osher and Sethian, 1988) has been widely used in shape-optimization problems due to its ability in automatic handling of changes in connectivities and interfaces. This method was first used for inverse obstacle problems in Santosa (1996), and thereafter, it was applied to a variety of inverse problems; see Litman et al. (1998); Osher and Santosa (2001); Hou et al. (2004); Dorn and Lesselier (2006); Miled and Miller (2007); van den Doel et al. (2010), and references therein. In terms of geophysical inverse problems, the level-set method has also found wide applications. In Isakov et al. (2011), the level-set method was first applied to the gravity data, and it was further developed in Isakov et al. (2013) and Lu et al. (2015); in Lu and Qian (2015) the level-set method was applied to the gravity gradient data. In Dorn and Villegas (2007) and Dorn and Ascher (2007), it was applied to shape reconstructions in 3-D electromagnetic induction tomography problems. In Samuel and Evonuk (2010) and Hillebrand et al. (2014), it was applied to geodynamical flow problems. In Papadopoulos et al. (2011) it was applied to identify uncertainties in the shape of geophysical objects using temperature measurements. In Zheglova et al. (2013), Li and Leung (2013) and Li et al. (2014) it was applied to travel-time tomography problems in different settings. In Li et al. (2015) it was applied to 3-D inversion of magnetic data.

The rest of this paper is organized as follows. At first, we propose the level-set method for gravity inversion in salt imaging. Following that, we summarize the algorithm and discuss some implementation details. To demonstrate the effectiveness of our level-set algorithm, we carry out intensive numerical experiments, and we mainly work on the SEG/EAGE salt model (Aminzadeh, 1996), where both 2-D slices and the 3-D model are studied in the inversion. Finally, we draw our conclusion.

## METHODOLOGY

The gravity data in salt-structure imaging is the anomalous acceleration generated by the embedded salt body and measured along the vertical direction:

$$g_z(\tilde{\mathbf{r}}) = \gamma \int_{\Omega} K_z(\tilde{\mathbf{r}}, \mathbf{r}) \cdot \rho(\mathbf{r}) d\mathbf{r}, \quad \tilde{\mathbf{r}} \in \Gamma. \quad (1)$$

In equation 1,  $\mathbf{r} = (x, y, z)$ ,  $\rho(\mathbf{r})$  is the density contrast,  $\gamma$  is the universal gravitational constant and  $\gamma \equiv 6.67384 \times 10^{-8} \text{cm}^3 \text{g}^{-1} \text{s}^{-2}$ .  $K_z(\tilde{\mathbf{r}}, \mathbf{r})$  is the integration kernel with the following formula,

$$K_z(\tilde{\mathbf{r}}, \mathbf{r}) = -\frac{\tilde{z} - z}{|\tilde{\mathbf{r}} - \mathbf{r}|^n}, \quad (2)$$

where  $n = 3$  in the 3-D space and  $n = 2$  in the 2-D space. Using the gravity data  $g_z(\tilde{\mathbf{r}})$  collected on  $\Gamma$  we invert for the density contrast  $\rho(\mathbf{r})$  in  $\Omega$  that provides an image of the underlying salt structure. Figure 1 illustrates the geometry of the problem setup in the 2-D space.

### A level-set formulation for the density contrast

To overcome the difficulties of salt imaging by gravity inversion associated with nil zone and the effect of annihilator, we incorporate a prior geological information into the formulation of density contrast so that we look for a depth-dependent density contrast in the following form

$$\rho(\mathbf{r}) = \begin{cases} \Delta\rho(z) & , \quad \mathbf{r} \in \Omega_0 \\ 0 & , \quad \mathbf{r} \in \Omega \setminus \Omega_0 \end{cases} \quad (3)$$

where  $\Omega_0$  denotes the region of a salt body, and  $\Delta\rho(z)$  is the assumed density contrast between the salt body and the sedimentary host at depth  $z$ . We assume that the value of  $\Delta\rho(z)$  is known due to some a prior geological information, and we solve for the unknown region  $\Omega_0$  so as to recover the shape of the embedded salt body. The strategy of imposing a priori information on the density contrast is widely acknowledged in gravitational salt-imaging (Barbosa et al., 1999; Jorgensen and

Kisabeth, 2000; Cheng et al., 2003; Krahenbuhl and Li, 2006). Equation 3 is the same binary formulation as adopted in Krahenbuhl and Li (2006). In this paper, however, we propose to handle the binary formulation in a continuous level-set framework so that we can apply a derivative-based optimization strategy to recover the binary structure.

Following the methodology proposed in Isakov et al. (2011), Lu and Qian (2015) and Li et al. (2015), we express the density contrast  $\rho(\mathbf{r})$  in equation 3 using the following level-set formulation,

$$\rho(\mathbf{r}) = H(\phi(\mathbf{r})) \cdot \Delta\rho(z), \quad \mathbf{r} \in \Omega. \quad (4)$$

In equation 4,  $H(x)$  is the Heaviside function with

$$H(x) = \begin{cases} 1 & , \quad x > 0 \\ 0.5 & , \quad x = 0 \\ 0 & , \quad x < 0 \end{cases}$$

$\phi(\mathbf{r})$  is the level-set function:

$$\phi(\mathbf{r}) = \begin{cases} > 0 & , \quad \mathbf{r} \in \Omega_0^{\text{int}} \\ = 0 & , \quad \mathbf{r} \in \partial\Omega_0 \\ < 0 & , \quad \mathbf{r} \in \Omega \setminus \overline{\Omega}_0 \end{cases}$$

where  $\Omega_0^{\text{int}}$ ,  $\overline{\Omega}_0$ , and  $\partial\Omega_0$  are the interior, closure, and boundary of domain  $\Omega_0$ , respectively. Numerically the level-set function is maintained to be the signed-distance function to the interface between  $\Omega_0$  and  $\Omega \setminus \Omega_0$ ,

$$\phi(\mathbf{r}) = \begin{cases} \text{dist}(\mathbf{r}, \partial\Omega_0) & , \quad \mathbf{r} \in \Omega_0 \\ -\text{dist}(\mathbf{r}, \partial\Omega_0) & , \quad \mathbf{r} \in \Omega \setminus \Omega_0 \end{cases}$$

where  $\text{dist}(\mathbf{r}, \partial\Omega_0)$  is the shortest distance from  $\mathbf{r}$  to  $\partial\Omega_0$ . As a specific example considering that

the interface  $\partial\Omega_0$  is a spherical surface of radius 1, the corresponding signed-distance function is

$$\phi(\mathbf{r}) = 1 - \sqrt{(x - x_0)^2 + (y - y_0)^2 + (z - z_0)^2}$$

with  $(x_0, y_0, z_0)$  the center of the sphere. The signed-distance property can be maintained by the level-set reinitialization, which will be discussed in the ALGORITHM section. The level-set function  $\phi(\mathbf{r})$  is continuous and parameterizes the unknown region  $\Omega_0$  so that equation 4 enables us to handle the binary density contrast  $\rho(\mathbf{r})$  by evaluating the continuous function  $\phi(\mathbf{r})$ . We can compute the sensitivity of  $\rho(\mathbf{r})$  with respect to the level-set function by the following variational formulation,

$$\frac{\partial \rho}{\partial \phi}(\mathbf{r}) = H'(\phi) \cdot \Delta \rho(z) = \delta_d(\phi(\mathbf{r})) \cdot \Delta \rho(z), \quad \mathbf{r} \in \Omega, \quad (5)$$

where  $\delta_d(x)$  is the Dirac-delta function.

Next we apply a derivative-based optimization method to recover the level-set function  $\phi(\mathbf{r})$ .

## A gradient-descent method for gravity inversion

Given an arbitrary density contrast, let  $g_z$  be the predicted data from the forward model in equation 1. Denoting the observed gravity data by  $g_z^*$ , we propose to find the targeted unknown density contrast by minimizing the data misfit function

$$E_d = \frac{1}{2} \int_{\Gamma} (g_z - g_z^*)^2 d\tilde{\mathbf{r}}. \quad (6)$$

Plugging equation 1 into equation 6 we can compute the sensitivity of  $E_d$  with respect to the density contrast,

$$\frac{\partial E_d}{\partial \rho}(\mathbf{r}) = \gamma \int_{\Gamma} (g_z(\tilde{\mathbf{r}}) - g_z^*(\tilde{\mathbf{r}})) \cdot K_z(\tilde{\mathbf{r}}, \mathbf{r}) d\tilde{\mathbf{r}}, \quad (7)$$

where  $K_z(\tilde{\mathbf{r}}, \mathbf{r})$  is defined in equation 2. Then combining equation 5 and equation 7 we get the sensitivity function of  $E_d$  with respect to the level set function  $\phi$ ,

$$\frac{\partial E_d}{\partial \phi}(\mathbf{r}) = \frac{\partial E_d}{\partial \rho} \cdot \frac{\partial \rho}{\partial \phi} = \delta_d(\phi(\mathbf{r})) \cdot \Delta \rho(z) \cdot \gamma \int_{\Gamma} (g_z(\tilde{\mathbf{r}}) - g_z^*(\tilde{\mathbf{r}})) \cdot K_z(\tilde{\mathbf{r}}, \mathbf{r}) d\tilde{\mathbf{r}}. \quad (8)$$

The necessary condition for  $\phi$  to be a minimizer is that  $\frac{\partial E_d}{\partial \phi} = 0$ . We adopt the gradient-descent method to evaluate the minimizer,

$$\begin{aligned} \frac{\partial \phi}{\partial t} &= -\frac{\partial E_d}{\partial \phi} && \text{in } \Omega, \\ \frac{\partial \phi}{\partial \mathbf{n}} &= 0 && \text{on } \partial\Omega, \end{aligned} \quad (9)$$

where a Neumann boundary condition is imposed on the computational domain. The solution of gravity inversion is obtained when the steady state of equation 9 is achieved; namely,  $\frac{\partial \phi}{\partial t} = 0$ .

Although the computation is in a continuous framework using a gradient-descent-based optimization method, the recovered density contrast in equation 4 has a binary structure with sharp interface indicating the shape of a salt body.

### **The strategy of incorporating the known top of a salt body into the inversion**

In geophysical exploration the top of a salt body is usually well imaged by seismic methods, and it can be used as a prior information in the gravity inversion (Li, 2001; Cheng et al., 2003). In this subsection, we introduce a simple strategy to incorporate the knowledge of the top of a salt body into our level-set inversion.

Supposing that the top of a salt body in the shallow region  $\{z \leq z_0\}$  is available from other imaging methods, we are trying to reconstruct the density contrast  $\rho(\mathbf{r})$  in the sub-domain  $\{z > z_0\}$ . The idea is to exclude the effects of the top of the salt body and perform inversion in the base

region. First we compute the gravity acceleration generated by the known top of the salt body,

$$g_{\text{top}}(\tilde{\mathbf{r}}) = \gamma \int_{\Omega \cap \{z \leq z_0\}} K_z(\tilde{\mathbf{r}}, \mathbf{r}) \cdot \rho(\mathbf{r}) d\mathbf{r}, \quad \tilde{\mathbf{r}} \in \Gamma. \quad (10)$$

Then we subtract  $g_{\text{top}}(\tilde{\mathbf{r}})$  from the observed gravity data  $g_z^*(\tilde{\mathbf{r}})$  and denote  $\overline{g}_z^*(\tilde{\mathbf{r}}) = g_z^*(\tilde{\mathbf{r}}) - g_{\text{top}}(\tilde{\mathbf{r}})$ .

Combining equation 10 and equation 1, it is straightforward to get the following expression,

$$\overline{g}_z^*(\tilde{\mathbf{r}}) = g_z^*(\tilde{\mathbf{r}}) - g_{\text{top}}(\tilde{\mathbf{r}}) = \gamma \int_{\Omega \cap \{z > z_0\}} K_z(\tilde{\mathbf{r}}, \mathbf{r}) \cdot \rho(\mathbf{r}) d\mathbf{r}, \quad \tilde{\mathbf{r}} \in \Gamma,$$

which indicates that  $\overline{g}_z^*(\tilde{\mathbf{r}})$  are the anomalous acceleration generated by the base of the salt body in the sub-domain  $\{z > z_0\}$ . Using these new data we perform the level-set inversion in the sub-domain  $\Omega \cap \{z > z_0\}$ , which yields an effective algorithm for reconstructing the base of the salt body. In our numerical simulations, we will show inversion results with and without a prior information of the top of a salt body.

## ALGORITHM

In this section we summarize the level-set algorithm for salt imaging.

Algorithm: a level-set method for salt imaging

1. Initialize the level-set function  $\phi$ .
2. Obtain the density function  $\rho(\mathbf{r})$  according to equation 4, and compute the predicted gravity data  $g_z(\tilde{\mathbf{r}})$  according to equation 1.
3. Compute the gradient flow  $\frac{\partial E_d}{\partial \phi}$  according to equation 8.
4. Evolve the level-set function  $\phi$  according to equation 9.
5. Reinitialize the level-set function to maintain the signed distance property.

6. Go back to step 2 until the iteration converges.

---

The Dirac-delta function  $\delta_d(\phi)$  appearing in equation 8 is numerically evaluated by

$$(\delta_d)_\epsilon(\phi) = \mathcal{I}_{T_\epsilon} \cdot |\nabla \phi|$$

(Zhao et al., 1996; Lu et al., 2015; Lu and Qian, 2015; Li et al., 2015), where

$$\mathcal{I}_{T_\epsilon}(\mathbf{r}) = \begin{cases} 1 & , \quad \mathbf{r} \in T_\epsilon \\ 0 & , \quad \mathbf{r} \in \Omega \setminus T_\epsilon \end{cases}$$

with the support  $T_\epsilon = \{\mathbf{r} \in \Omega : |\phi(\mathbf{r})| < \epsilon\}$ . The parameter  $\epsilon$  controls the bandwidth of the delta impulsive function, and we set it to be  $0.5 \cdot \min\{\Delta x, \Delta y, \Delta z\}$  in the numerical simulation.

The gradient flow in equation 8 is expressed as

$$\frac{\partial E_d}{\partial \phi} = V \cdot |\nabla \phi|,$$

where

$$V = \mathcal{I}_{T_\epsilon}(\mathbf{r}) \cdot \Delta \rho(z) \cdot \gamma \int_{\Gamma} (g_z(\tilde{\mathbf{r}}) - g_z^*(\tilde{\mathbf{r}})) \cdot K_z(\tilde{\mathbf{r}}, \mathbf{r}) d\tilde{\mathbf{r}}.$$

Therefore the evolution equation 9 in step 4 is reduced to the following form

$$\frac{\partial \phi}{\partial t} = -V \cdot |\nabla \phi|,$$

which can be viewed as a Hamilton-Jacobi equation (Osher and Sethian, 1988; Osher and Shu, 1991; Jiang and Peng, 2000; Qian and Symes, 2002; Cecil et al., 2004). We simply apply forward-differencing to the time derivative and central-differencing to the spatial derivatives, and the level-

set function  $\phi$  is updated by the equation

$$\phi^{n+1} = \phi^n - \Delta t \cdot V^n \cdot (|\nabla \phi|)^n. \quad (11)$$

In equation 11 the superscript  $n$  means the value at the  $n$ -th step. Numerically a Courant-Friedrichs-Lowy (CFL) stability condition is required to maintain the stability of evolution,

$$\Delta t \cdot \left( \frac{\max |V^n|}{\min \{\Delta x, \Delta y, \Delta z\}} \right) < 1.$$

In practice we take the time step

$$\Delta t = \alpha \cdot \frac{\min \{\Delta x, \Delta y, \Delta z\}}{\max |V^n|} \quad (12)$$

where  $\alpha$  is a constant between 0 and 1. In practice, we have chosen  $\alpha = 0.8$  for 2-D examples and  $\alpha = 0.6$  for 3-D examples. This choice of  $\alpha$  only affects computational time but not accuracy.

To evaluate the integrals in equation 1 and equation 8, we have developed a low-rank matrix-decomposition algorithm to speed up matrix-vector multiplications arising in the numerical integration; one can find detailed formulations in Lu et al. (2015) and Li et al. (2015).

Moreover, in step 5 we reinitialize the level-set function to maintain the signed-distance property for  $\phi$ . In the level-set evolution the function  $\phi$  can develop steep gradients and non-smooth features that are not amenable to finite-difference approximations. Therefore, it is always desirable to reinitialize the level-set function occasionally so that  $\phi$  stays smooth (Osher and Sethian, 1988; Mulder et al., 1992; Sussman et al., 1994). To achieve this we reinitialize  $\phi$  to be a signed-distance function, since the signed-distance property preserves the zero level-set which parameterizes the shape of the underlying interface. Mathematically, it can be achieved by solving the following

system in an artificial time-direction  $\xi$  up to the steady state

$$\frac{\partial \Phi}{\partial \xi} + \text{sign}(\phi) \cdot (|\nabla \Phi| - 1) = 0, \quad (13)$$

$$\left. \frac{\partial \Phi}{\partial n} \right|_{\partial \Omega} = 0, \quad (14)$$

where the initial condition is  $\Phi|_{\xi=0} = \phi$  and the function  $\text{sign}(\cdot)$  is the signum function which extracts the sign of a real number (Sussman et al., 1994). In practice, however, since we are interested in the solution only near the zero level-set, there is no need to obtain the actual steady-state solution. Instead, we simply solve the system for several  $\Delta \xi$  steps (in our numerical simulation only one step) and the intermediate solution  $\Phi$  is used to replace the original level-set function. Since the reinitialization procedure smoothens the level-set function, it can be viewed as a regularization on the model parameter  $\phi$ . One can find applications of this technique in Isakov et al. (2011, 2013); Li and Leung (2013); Li et al. (2014, 2015).

## NUMERICAL EXPERIMENTS

In this section we demonstrate the effectiveness of the proposed level-set method for salt imaging. We work on the SEG/EAGE salt model (Aminisadeh, 1996); both 2-D slices and 3-D full structures of the salt model will be studied in the inversion.

The original SEG/EAGE salt model is a velocity model designed to challenge contemporary seismic imaging methods. To validate our new algorithm for gravity inversion, we have captured the structure of the salt body, and accordingly we have constructed the following density-contrast model, still named SEG/EAGE salt model. The profile of the salt body is shown in Figure 2. The computational domain is set to be  $\Omega = [0, 13\,400]\text{m} \times [0, 13\,400]\text{m} \times [0, 4\,000]\text{m}$ . Two sets of expected density contrasts  $\Delta\rho(z)$  are considered. Following the setup in Krahnenbuhl and Li (2006), we

specify the first set of density contrast  $\Delta\rho(z)$  to be

$$\Delta\rho(z) = \begin{cases} 0.2 \text{ g} \cdot \text{cm}^{-3} & , z \leq 1800 \text{ m} \\ -0.2 \text{ g} \cdot \text{cm}^{-3} & , z > 1800 \text{ m} \end{cases}. \quad (15)$$

Above 1800 m the salt body has a positive density contrast whereas below that depth the salt body has a negative density contrast. The density-contrast reversal simulates the effect of annihilator in salt imaging. To further simulate realistic scenarios in salt imaging, we specify the second set of density contrast to be

$$\Delta\rho(z) = \frac{1800 - z}{1000} \times 0.2 \text{ g} \cdot \text{cm}^{-3}. \quad (16)$$

so that the density contrast between the salt body and its sediments is linearly decreasing in depth, which corresponds to the scenario where the background density distribution increases in depth and the density of the salt body is constant.

## 2-D examples

We start the computation from 2-D structures. A cross-section of the 3-D SEG/EAGE salt model shown in Figure 1 is studied in this subsection. The slice is taken along the plane defined by the three points:  $A_1(0\text{m}, 2200\text{m}, 0\text{m})$ ,  $A_2(13400\text{m}, 6600\text{m}, 0\text{m})$  and  $A_3(13400\text{m}, 6600\text{m}, 4000\text{m})$ ; Figure 3a and Figure 6a display the shape of the exact structure. The 2-D section has a crest of positive density contrast located on the top of the salt body and a steeply dipping flank of negative density contrast extending to a large depth. We test two sets of density contrasts given by formula 15 and formula 16 respectively.

### *A 2-D slice with a piecewise-constant density contrast*

In this example we consider the cross-section with a density contrast given by equation 15. The exact structure is shown in Figure 3a, where the 2-D domain  $\Omega_{2D} = [0, 13400]\text{m} \times [0, 4000]\text{m}$  is

uniformly discretized into  $671 \times 201$  mesh points. The gravity data  $g_z^*$  are collected along a 40km survey line  $\Gamma = [-13000, 27000]\text{m} \times \{z = -100\}\text{m}$ , and there are 41 observation points uniformly distributed on  $\Gamma$ ; Figure 3b displays the exact (simulated) gravity data. To perform the inversion, we start from an initial guess as shown in Figure 3c, where the shape of the initial structure is an ellipse with the semi-major axis of 4000m and the semi-minor axis of 1000m. We evolve the level-set function according to equation 11, and the time step is given by formula 12 with  $\alpha = 0.8$ . Figure 3e plots the misfit function  $E_d$  versus the number of iterations. The convergence is achieved when there is no further reduction in the misfit function. Due to nonlinearity of the inverse problem, the convergence history of the misfit function shows an oscillating pattern. Since it is difficult to maintain a monotonic convergence even by implementing an expensive line search, we dismiss that option here. The large number of iterations in this example are due to the CFL condition in the evolving direction of the gradient descent flow. Figure 3d shows the recovered structure after 50000 iterations. The top of the salt body with positive density contrast is well imaged in the recovered solution, and the shape of the crest matches well with the exact structure. The lower portion of the salt body is also successfully captured in the recovered solution. The steeply dipping flank extending to the left is partially recovered, though the base structure is distorted due to the limited resolution of the gravity inversion.

To explore the possibility of recovering full structure of the dipping flank, we freeze the top of the salt body and perform the inversion in the base region; specifically we impose the exact structure to the salt body above 1800 m. First we compute the gravity acceleration generated by the salt body above 1800 m according to equation 10, and we subtract this acceleration from the observed gravity data  $g_z^*$  so that the resulting data yield the gravity acceleration induced by the base structure below 1800 m. We apply our inversion algorithm to these new data in the sub-domain  $\{z > 1800 \text{ m}\}$ . This strategy not only remarkably reduces the computational cost but also significantly improves the resolution of the inversion result. Figure 4 demonstrates the numerical results. Figure 4a shows the initial guess of the level-set function  $\phi$ , which is constructed in the

following way; in the inversion domain  $\{z > 1800 \text{ m}\}$  we define the function

$$\phi_0(x, z) = \begin{cases} 0.5\Delta x & , (x, 1800 \text{ m}) \in \text{salt} \& z \leq 2500 \text{ m} \\ -0.5\Delta x & , \text{otherwise} \end{cases},$$

and we perform the level-set reinitialization on  $\phi_0$  to produce the initial guess of  $\phi$ . Figure 4b displays the complete initial structure, and the initial guess is a natural extension of the top of the salt body along the  $z$ -direction. The level-set function is evolved in the sub-domain  $\{z > 1800 \text{ m}\}$ , and the time step is still given by formula 12 with  $\alpha = 0.8$ . Figure 4e shows the convergence history; the misfit function steadily oscillates in the order of  $10^{-4}$  when the convergence is achieved. The recovered structure after 1500 iterations is shown in Figure 4d, where the steeply dipping flank is fully recovered in the base region. We mention that the CPU time required for this inversion is about 215 seconds on an equivalent 2.5 GHz processor.

To further test the robustness of the algorithm, we perturb the measured gravity data by 5% Gaussian noise, as shown in Figure 5a, and repeat the inversion process. Figure 5b shows the solution after 1500 iterations. The top of the salt body is frozen to be the exact structure and the steeply dipping flank is successfully recovered in the base region. Since the solution is similar to the recovered solution using clean measurements as shown in Figure 4d, our inversion algorithm is not sensitive to a small amount of additive Gaussian noise with zero mean.

#### *A 2-D slice with a linearly decreasing density contrast*

In this example we study a cross-section of the salt model with the density contrast given by equation 16. Figure 6a shows the exact structure, where the linearly decreasing density contrast simulates the salt body with a constant density embedded in a sedimentary background which density increases with depth due to compaction. The 2-D domain  $\Omega_{2D} = [0, 13400] \text{ m} \times [0, 4000] \text{ m}$  is uniformly discretized into  $671 \times 201$  mesh points. The gravity data are generated with 41 stations distributed along the survey line  $\Gamma = [-13000, 27000] \text{ m} \times \{z = -100\} \text{ m}$ , as shown in Figure 6b. To

perform the inversion, we set the initial guess to be an ellipse with the semi-major axis of 4000m and the semi-minor axis of 1000m, which is shown in Figure 6c. The level-set function is evolved according to equation 11, and the time step is given by formula 12 with  $\alpha = 0.8$ . Figure 6e shows the convergence history; the misfit function steadily oscillates around  $10^{-5}$  when the convergence is achieved. Figure 6d plots the recovered solution after 50000 iterations. The top of the salt body is well imaged with a crest matching well with the exact structure. The lower portion with negative density contrast is also successfully captured. The recovered solution provides useful information for interpreting the structure of the steeply dipping flank, though the overall shape is distorted to some extent due to the limited resolution of the gravity inversion.

To pursue better resolution for the steeply dipping flank we freeze the top of the salt body and impose the exact structure to the salt body above 1800 m. The top of the salt body is assumed to be available from seismic imaging, which can be used as a prior information in the gravity inversion. In the example with piecewise-constant density contrast, we demonstrated that adding constraints to the top of the salt body does improve resolution of deep structures. Here we use the same strategy: we remove the effect of the top of the salt body and perform the inversion algorithm in the sub-domain  $\{z > 1800 \text{ m}\}$ . Figure 7a shows the initial guess of the level-set function, which is the same as Figure 4a. Figure 7b displays the initial structure in the full domain, and the initial guess is a natural extension of the top of the salt body. The level-set function is evolved in the sub-domain  $\{z > 1800 \text{ m}\}$ , and the time step is given by formula 12 with  $\alpha = 0.8$ . Figure 7e plots the misfit function  $E_d$  versus the number of iterations. The misfit function steadily oscillates in the order of  $10^{-4}$  when the convergence is achieved. Figure 7d shows the recovered solution after 2000 iterations. The steeply dipping flank is successfully recovered, and the overall shape matches well with the exact structure. We mention that the CPU time for this inversion is approximately 288 seconds on an equivalent 2.5 GHz processor.

To study the effect of noise we contaminate the clean measurements with 5% Gaussian noise and repeat the inversion process with the top of the salt body constrained to be the exact structure. Figure 8a displays the noisy gravity data; Figure 8b shows the recovered solution. There is no

big distortion in the recovered structure, and the inversion is not sensitive to a small amount of Gaussian noise with zero mean.

### The 3-D SEG/EAGE salt model

In this example we work on the 3-D SEG/EAGE salt model with a linearly decreasing density contrast. The shape of the salt body is displayed in Figure 9a and 9c (also in Figure 2), and the density contrast  $\Delta\rho(z)$  is given by equation 16. The linearly decreasing density contrast simulates the effect of annihilator in salt imaging. The gravity data  $g_z^*$  are generated along the measurement surface  $\Gamma = [-13000, 27000]\text{m} \times [-13000, 27000]\text{m} \times \{z = -100\}\text{m}$ . There are  $41 \times 41 = 1681$  stations uniformly distributed on  $\Gamma$  and the observed data are shown in Figure 9f. To perform the inversion, we discretize the computational domain into  $68 \times 68 \times 21$  mesh points and start from the initial guess as shown in Figure 9e. The initial guess is an oblate spheroid with the semi-major axis of 4000 m and the semi-minor axis of 1000 m. We evolve the level-set function according to equation 11, and the time step is given by formula 12 with  $\alpha = 0.6$ . The recovered solution is shown in Figure 9b and Figure 9d from different angles of view. We mention that the required CPU time for this inversion is about 44 minutes on an equivalent 2.5 GHz processor.

In the recovered solution the top of the salt body is well imaged with the peak successfully recovered from the flat surface in the initial guess, and the stratum structure is well captured. The dipping flank to large depth is also recovered in the reconstruction, though there is distortion in the deep region due to the poor depth resolution of gravity inversion; the lateral view displayed in Figure 9d illustrates the shape of the dipping flank. To see the result more clearly we also provide the pictures of cross-sections in Figure 10 and Figure 11. Cross-sections of the underlying structure are displayed at  $y = 4000\text{ m}, 6000\text{ m},$  and  $8000\text{ m}$  and  $x = 6000\text{ m}, 8000\text{ m},$  and  $10000\text{ m}$ , respectively. Generally the reconstruction has better resolution in the top of the salt body, while the deep structure with reverse density contrast is also successfully captured. Our level-set algorithm provides an effective method for salt imaging in the presence of density-contrast reversal.

To further test the robustness of our level-set algorithm, we add 2% Gaussian noise with zero mean to the measurement data  $g_z^*$  and repeat the inversion process. Figure 12f shows the contaminated gravity data. Figures 12b and 12d show the recovered solution after 8000 iterations. We also display the cross-sections of the inverted structure in Figures 13 and 14. The solution is quite similar to the recovered solution using clean measurements, as shown in Figures 9, 10 and 11. The general structure of the salt body is well recovered; the crest of the salt body matches well with the exact structure; the dipping flank to large depth is also partially recovered, which provides useful information for interpreting the base of the salt body. These results, therefore, illustrate that our level-set algorithm has the potential to handle realistic salt-imaging problems in the presence of reasonable noise contamination.

In the end of this section, we study the effect of adding constraints to the top of the salt body in the SEG/EAGE 3-D salt model. The purpose is to explore the possibility of recovering delicate features at the base of the salt body. Following the same strategy as used in 2-D examples, we impose the exact structure to the salt body above 1800 m and perform the inversion in the sub-domain  $\{z > 1800 \text{ m}\}$ . First we subtract the gravity acceleration generated by the salt body above 1800 m from the observed gravity data  $g_z^*$ , and the results yield the acceleration generated by the base of the salt body below 1800 m. Using the new data we evolve the level-set function in the sub-domain  $\{z > 1800 \text{ m}\}$ ; the time step in the iteration is given by formula 12 with  $\alpha = 0.6$ . The initial guess of the level-set function is

$$\phi(x, y, z) = 1 - \sqrt{\left(\frac{x - 7000}{2000}\right)^2 + \left(\frac{y - 7000}{2000}\right)^2 + \left(\frac{z - 2000}{1000}\right)^2}, \quad z > 1800.$$

Figures 15a and 15b display the initial structure from different angles of view, where the top of the salt body is enforced to be the exact structure and the base of the salt body is initialized to be a half ellipsoid. Figure 16 shows the recovered solution after 200 iterations, where the solution is displayed from three different angles of view. Basically the steeply dipping flank is successfully recovered in the base region, though there is still imperfection in the shape of the dipping flank.

Adding constraints to the top of the salt body does improve the resolution of imaging at the base of the salt body. The CPU time required for this inversion is about 184 seconds on an equivalent 2.5 GHz processor. Figure 17 shows the history of convergence, where the misfit function oscillates steadily around  $5 \times 10^{-2}$  when the convergence is achieved.

We also carry out constrained inversion using the data contaminated by 2% Gaussian noise, as shown in Figure 12f. Figure 19 shows the convergence history and Figures 18b, 18d and 18f display the solution after 200 iterations. There is no big distortion in the recovered structure comparing to the solution using clean measurements, as shown in Figures 16b, 16d and 16f, and the level-set algorithm can handle salt-imaging problems in the presence of reasonable noise contamination.

## CONCLUSIONS

In this paper we have proposed a level-set algorithm for salt imaging using gravity data. To handle the problem of nil zone and the effect of annihilator, we have adopted a binary formulation for density contrast and inverted for a binary structure of the salt body. The level-set method has been applied to manipulate the binary structure in a continuous framework. In contrast to working on the binary density contrast directly, the proposed algorithm looks for a level-set function which is maintained to be continuous in the inversion. The advantage of the level-set algorithm is that we can reconstruct the binary structure using a gradient-descent-based optimization method. Numerical examples demonstrated the effectiveness of our algorithms, and we have efficiently recovered 3-D salt structures generated from the SEG/EAGE salt model. We believe that the proposed algorithms can be further accelerated by implementing more efficient optimization methods.

## ACKNOWLEDGMENT

We thank assistant editor Dr. Jeffrey Shragge and associate editor Dr. Xiong Li for careful handling of our paper. We also thank Dr. Yaoguo Li, Dr. Michael Zhdanov, and two additional anonymous reviewers for their constructive and valuable comments and suggestions. Qian is supported by

National Science Foundation grants 1222368, 1439979 and 1522249.

## REFERENCES

- Aminsadeh, F., 1996, 3-D salt and overthrust seismic models: AAPG Studies in Geology No. 42 and SEG Geophysical Developments Series No. 5.
- Bain, J. E., Weyand, J., and Weber, M., Resolving complex salt features using gravity and magnetism: AAPG Invited Lecture Series, 1991.
- Bain, J. E., Horscroft, T. R., Weyand, J., Saad, A. H., and Bulling, D. N., 1993, Complex salt features resolved by integrating seismic, gravity and magnetics: EAEG/EAPG Annual Meeting, Expanded Abstracts.
- Barbosa, V. C. F., Silva, J. B. C., and Medeiros, W. E., 1999, Gravity inversion of a discontinuous relief stabilized by weighted smoothness constraints on depth: *Geophysics*, **64**, no. 5, 1429–1437.
- Barnes, G. J., and Barraud, J., 2012, Imaging geologic surfaces by inverting gravity gradient data with depth horizons: *Geophysics*, **77**, no. 1, G1–G11.
- Cai, H., and Zhdanov, M., 2015, Application of Cauchy-type integrals in developing effective methods for depth-to-basement inversion of gravity and gravity gradiometry data: *Geophysics*, **80**, no. 2, G81–G94.
- Cecil, T., Qian, J., and Osher, S. J., 2004, Numerical methods for high dimensional Hamilton-Jacobi equations using radial basis functions: *Journal of Computational Physics*, **196**, no. 1, 327–347.
- Cheng, D., Li, Y., and Larner, K., 2003, Inversion of gravity data for base salt: 74th Ann. Internat. Mtg., Soc. Expl. Geophys., Tulsa, OK, Expanded Abstracts, 1351–1354.
- Dorn, O., and Ascher, U., 2007, Shape reconstruction in 3-D electromagnetic induction tomography using a level set technique: Proc. 23rd International Review of Progress in Applied Computational Electromagnetics Conference ACES 2007, Verona, Italy.

Dorn, O., and Lesselier, D., 2006, Level set methods for inverse scattering: *Inverse Problems*, **22**, no. 4, R67–R131.

Dorn, O., and Villegas, R., 2007,, A level set method for 3-D low frequency electromagnetic imaging with applications in geophysical prospecting: *Proceedings in Applied Mathematics and Mechanics*, 6th International Congress on Industrial and Applied Mathematics, Zurich, Switzerland.

Ennen, C., and Hall, S., 2011, Structural mapping of the Vinton salt dome, Louisiana, using gravity gravimetry data: 82nd Ann. Internat. Mtg., Soc. Expl. Geophys., Tulsa, OK, Expanded Abstracts, 830–835.

Farmer, P., Miller, D., Pleprzak, A., Rutledge, J., and Woods, R., 1996, Exploring the subsalt: Oilfield Review, **8**, no. 1, 50–64.

Gibson, R. I., and Millegan, P. S., 1998, Geologic applications of gravity and magnetics: case histories: Published jointly by the Society of Exploration Geophysicists and the American Association of Petroleum Geologists.

Hatch, D., and Annechione, M., 2010, Gravity gradient interpretation of salt bodies in nil-zone regimes: 81st Ann. Internat. Mtg., Soc. Expl. Geophys., Tulsa, OK, Expanded Abstracts, 1127–1131.

Hillebrand, B., Thieulot, C., Geenen, T., Van Den Berg, A. P., and Spakman, W., 2014, Using the level set method in geodynamical modeling of multi-material flows and earth's free surface: *Solid Earth*, **5**, no. 2, 1087–1098.

Hou, S., Solna, K., and Zhao, H., 2004, Imaging of location and geometry for extended targets using the response matrix: *Journal of Computational Physics*, **199**, no. 1, 317–338.

Isakov, V., Leung, S., and Qian, J., 2011, A fast local level set method for inverse gravimetry: *Communications in Computational Physics*, **10**, no. 4, 1044–1070.

Isakov, V., Leung, S., and Qian, J., 2013, A three-dimensional inverse gravimetry problem for ice

with snow caps: *Inverse Problems and Imaging*, **7**, no. 2, 523–544.

Jiang, G. S., and Peng, D., 2000, Weighted ENO schemes for Hamilton-Jacobi equations: SIAM

*Journal on Scientific Computing*, **21**, no. 6, 2126–2143.

Jorgensen, G. J., and Kisabeth, J. L., 2000, Joint 3-D inversion of gravity magnetic and tensor

gravity fields for imaging salt formations in the deepwater Gulf of Mexico: 71st Ann. Internat.

Mtg., Soc. Expl. Geophys., Tulsa, OK, Expanded Abstracts, 424–426.

Krahenbuhl, R. A., and Li, Y., 2006, Inversion of gravity data using a binary formulation: *Geo-*

*physical Journal International*, **167**, no. 2, 543–556.

Leveille, J. P., Jones, I. F., Zhou, Z. Z., Wang, B., and Liu, F., 2011, Subsalt imaging for exploration,

production, and development: A review: *Geophysics*, **76**, no. 5, WB3–WB20.

Li, W., and Leung, S., 2013, A fast local level set adjoint state method for first arrival transmission

traveltime tomography with discontinuous slowness: *Geophysical Journal International*, **195**, no.

1, 582–596.

Li, Y., and Oldenburg, D. W., 1998, 3-D inversion of gravity data: *Geophysics*, **63**, no. 1, 109–119.

Li, W., Leung, S., and Qian, J., 2014, A level-set adjoint-state method for crosswell transmission-

reflection traveltome tomography: *Geophysical Journal International*, **199**, no. 1, 348–367.

Li, W., Lu, W., and Qian, J., 2015, A multiple level set method for three-dimensional inversion of

magnetic data: Submitted.

Li, Y., 2001, 3-D inversion of gravity gradiometer data: *Electrical and magnetic studies*, Depart-

ment Geophysics, Colorado School of Mines.

Litman, A., Lesselier, D., and Santosa, F., 1998, Reconstruction of a two-dimensional binary ob-

stacle by controlled evolution of a level-set: *Inverse Problems*, **14**, no. 3, 685–706.

- Lu, W., and Qian, J., 2015, A local level set method for three-dimensional inversion of gravity gradient data: *Geophysics*, **80**, no. 1, G35–G51.
- Lu, W., Leung, S., and Qian, J., 2015, An improved fast local level set method for three-dimensional inverse gravimetry: *Inverse Problems and Imaging*, **9**, no. 2, 479–509.
- Miled, M. B. H., and Miller, E. L., 2007, A projection-based level-set approach to enhance conductivity anomaly reconstruction in electrical resistance tomography: *Inverse Problems*, **23**, no. 6, 2375–2400.
- Mulder, W., Osher, S., and Sethian, J. A., 1992, Computing interface motion in compressible gas dynamics: *Journal of Computational Physics*, **100**, no. 2, 209–228.
- Oldenburg, D. W., Li, Y., Farquharson, C. G., Kowalczyk, P., Aravanis, T., King, A., Zhang, P., and Watts, A., 1998, Applications of geophysical inversions in mineral exploration: *The Leading Edge*, **17**, no. 4, 461–465.
- Osher, S. J., and Santosa, F., 2001, Level set methods for optimization problems involving geometry and constraints I. Frequencies of a two-density inhomogeneous drum: *Journal of Computational Physics*, **171**, no. 1, 272–288.
- Osher, S. J., and Sethian, J. A., 1988, Fronts propagating with curvature dependent speed: algorithms based on Hamilton-Jacobi formulations: *Journal of Computational Physics*, **79**, no. 1, 12–49.
- Osher, S. J., and Shu, C. W., 1991, High-order essentially non-oscillatory schemes for Hamilton-Jacobi equations: *SIAM Journal on Numerical Analysis*, **28**, no. 4, 907–922.
- Papadopoulos, D., Herty, M., Rath, V., and Behr, M., 2011, Identification of uncertainties in the shape of geophysical objects with level sets and the adjoint method: *Computational Geosciences*, **15**, no. 4, 737–753.

- Qian, J., and Symes, W. W., 2002, An adaptive finite difference method for traveltime and amplitude: *Geophysics*, **67**, no. 1, 167–176.
- Routh, P., Jorgensen, G., and Kisabeth, J., 2001, Base of the salt imaging using gravity and tensor gravity data: 72nd Ann. Internat. Mtg., Soc. Expl. Geophys., Tulsa, OK, Expanded Abstracts, 1482–1484.
- Samuel, H., and Evonuk, M., 2010, Modeling advection in geophysical flows with particle level sets: *Geochemistry, Geophysics, Geosystems*, **11**, no. 8, Q08020.
- Santosa, F., 1996, A level-set approach for inverse problems involving obstacles: *ESAIM: Control, Optimisation and Calculus of Variations*, **1**, 17–33.
- Silva Dias, F. J. S., Barbosa, V. C. F., and Silva, J. B. C., 2011, Adaptive learning 3D gravity inversion for salt body imaging: *Geophysics*, **76**, no. 3, I49–I57.
- Sussman, M., Smereka, P., and Osher, S. J., 1994, A level set approach for computing solutions to incompressible two-phase flows: *Journal of Computational Physics*, **114**, no. 1, 146–159.
- van den Doel, K., Ascher, U. M., and Leitao, A., 2010, Multiple level sets for piecewise constant surface reconstruction in highly ill-posed problems: *Journal of Scientific Computing*, **43**, no. 1, 44–66.
- Zhao, H. K., Chan, T., Merriman, B., and Osher, S., 1996, A variational level set approach to multiphase motion: *Journal of Computational Physics*, **127**, no. 1, 179–195.
- Zheglova, P., Farquharson, C. G., and Hurich, C. A., 2013, 2-D reconstruction of boundaries with level set inversion of traveltimes: *Geophysical Journal International*, **192**, no. 2, 688–698.

## LIST OF FIGURES

- 1 Geometry of the problem setup.
- 2 The density contrast model constructed from the SEG/EAGE salt model.
- 3 A 2-D slice of the SEG/EAGE salt model with piecewise-constant density contrast. (a) Exact model; (b) Gravity data; (c) Initial guess for the inversion algorithm; (d) Solution after 50000 iterations; (e) Misfit function versus iteration number.
- 4 A 2-D slice with a piecewise-constant density contrast; the top of the salt body is constrained and the computation is performed in the sub-domain  $\{z > 1800 \text{ m}\}$ . (a) Initial guess of the level-set function; (b) Initial structure in the full domain; (c) Exact model; (d) Recovered solution after 1500 iterations; (e) Misfit function versus iteration number.
- 5 A 2-D slice with a piecewise-constant density contrast; 5% Gaussian noise is added to the measurement. The top of the salt body is constrained and the computation is performed in the sub-domain  $\{z > 1800 \text{ m}\}$ . (a) Gravity data with 5% Gaussian noise; (b) Solution after 1500 iterations.
- 6 A 2-D slice of the SEG/EAGE salt model with a linearly decreasing density contrast. (a) Exact model; (b) Gravity data; (c) Initial guess for the inversion algorithm; (d) Solution after 50000 iterations; (e) Misfit function versus iteration number.
- 7 A 2-D slice with a linearly decreasing density contrast; the top of the salt body is constrained and the computation is performed in the sub-domain  $\{z > 1800 \text{ m}\}$ . (a) Initial guess of the level-set function; (b) Initial structure in the full domain; (c) Exact model; (d) Recovered solution after 2000 iterations; (e) Misfit function versus iteration number.
- 8 A 2-D slice with a linearly decreasing density contrast; 5% Gaussian noise is added to the measurement. The top of the salt body is constrained and the computation is performed in the sub-domain  $\{z > 1800 \text{ m}\}$ .
- 9 A 3-D SEG/EAGE salt model. (a) Exact model; (b) Solution after 8000 iterations; (c) Lateral view of the exact model; (d) Lateral view of the solution; (e) Initial guess for the inversion algorithm; (f) Gravity data.

10 A 3-D SEG/EAGE salt model. Cross-sections at  $y = 4000$  m,  $y = 6000$  m and  $y = 8000$  m of the exact and recovered model.

11 A 3-D SEG/EAGE salt model. Cross-sections at  $x = 6000$  m,  $x = 8000$  m and  $x = 10\,000$  m of the exact and recovered model.

12 A 3-D SEG/EAGE salt model with 2% Gaussian noise added to the measurement. (a) Exact model; (b) Solution after 8000 iterations; (c) Lateral view of the exact model; (d) Lateral view of the solution; (e) Initial guess for the inversion algorithm; (f) Gravity data.

13 A 3-D SEG/EAGE salt model with 2% Gaussian noise added to the measurement. Cross-sections at  $y = 4000$  m,  $y = 6000$  m and  $y = 8000$  m of the exact and recovered model.

14 A 3-D SEG/EAGE salt model with 2% Gaussian noise added to the measurement. Cross-sections at  $x = 6000$  m,  $x = 8000$  m, and  $x = 10\,000$  m of the exact and recovered model.

15 A 3-D SEG/EAGE salt model; the top of the salt body is constrained and the computation is performed in the sub-domain  $\{z > 1800$  m $\}$ . Display of the initial guess.

16 A 3-D SEG/EAGE salt model; the top of the salt body is constrained and the computation is performed in the sub-domain  $\{z > 1800$  m $\}$ . (a) The exact structure; (b) The recovered solution; (c) Lateral view of the exact structure along the  $x$ -axis; (d) Lateral view of the recovered solution along the  $x$ -axis; (e) Lateral view of the exact structure along the  $y$ -axis; (f) Lateral view of the recovered solution along the  $y$ -axis.

17 A 3-D SEG/EAGE salt model; the top of the salt body is constrained and the computation is performed in the sub-domain  $\{z > 1800$  m $\}$ . History of convergence.

18 A 3-D SEG/EAGE salt model with 2% Gaussian noise added to the measurement; the top of the salt body is constrained and the computation is performed in the sub-domain  $\{z > 1800$  m $\}$ . (a) The exact structure; (b) The recovered solution; (c) Lateral view of the exact structure along the  $x$ -axis; (d) Lateral view of the recovered solution along the  $x$ -axis; (e) Lateral view of the exact structure along the  $y$ -axis; (f) Lateral view of the recovered solution along the  $y$ -axis.

19 A 3-D SEG/EAGE salt model with 2% Gaussian noise added to the measurement; the top of the salt body is constrained. History of convergence.

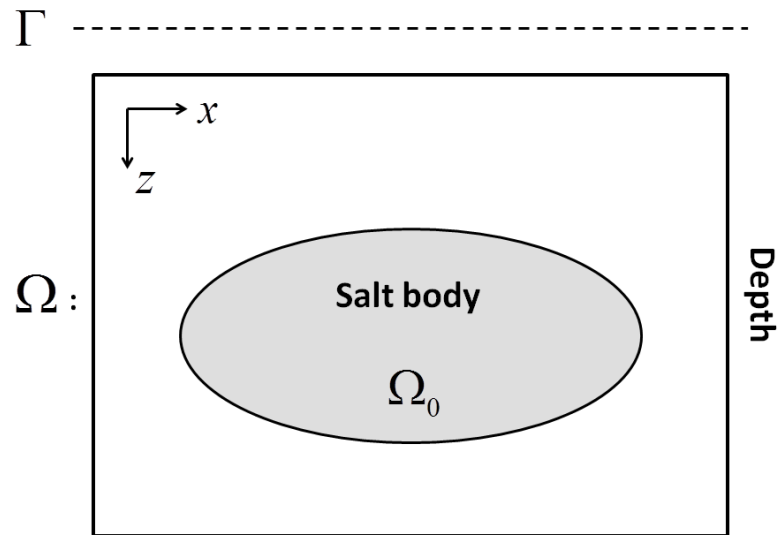


Figure 1: Geometry of the problem setup.

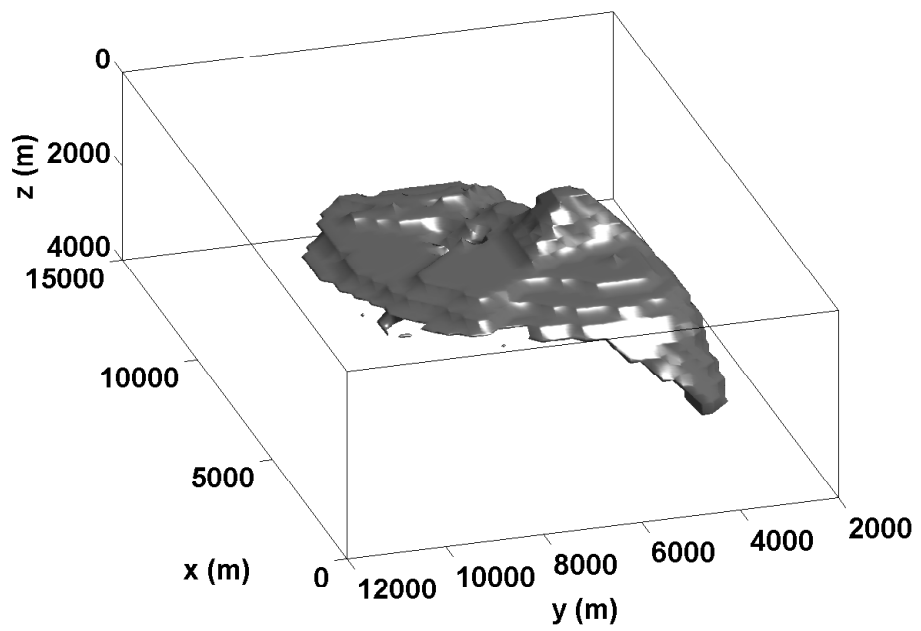


Figure 2: The density contrast model constructed from the SEG/EAGE salt model.

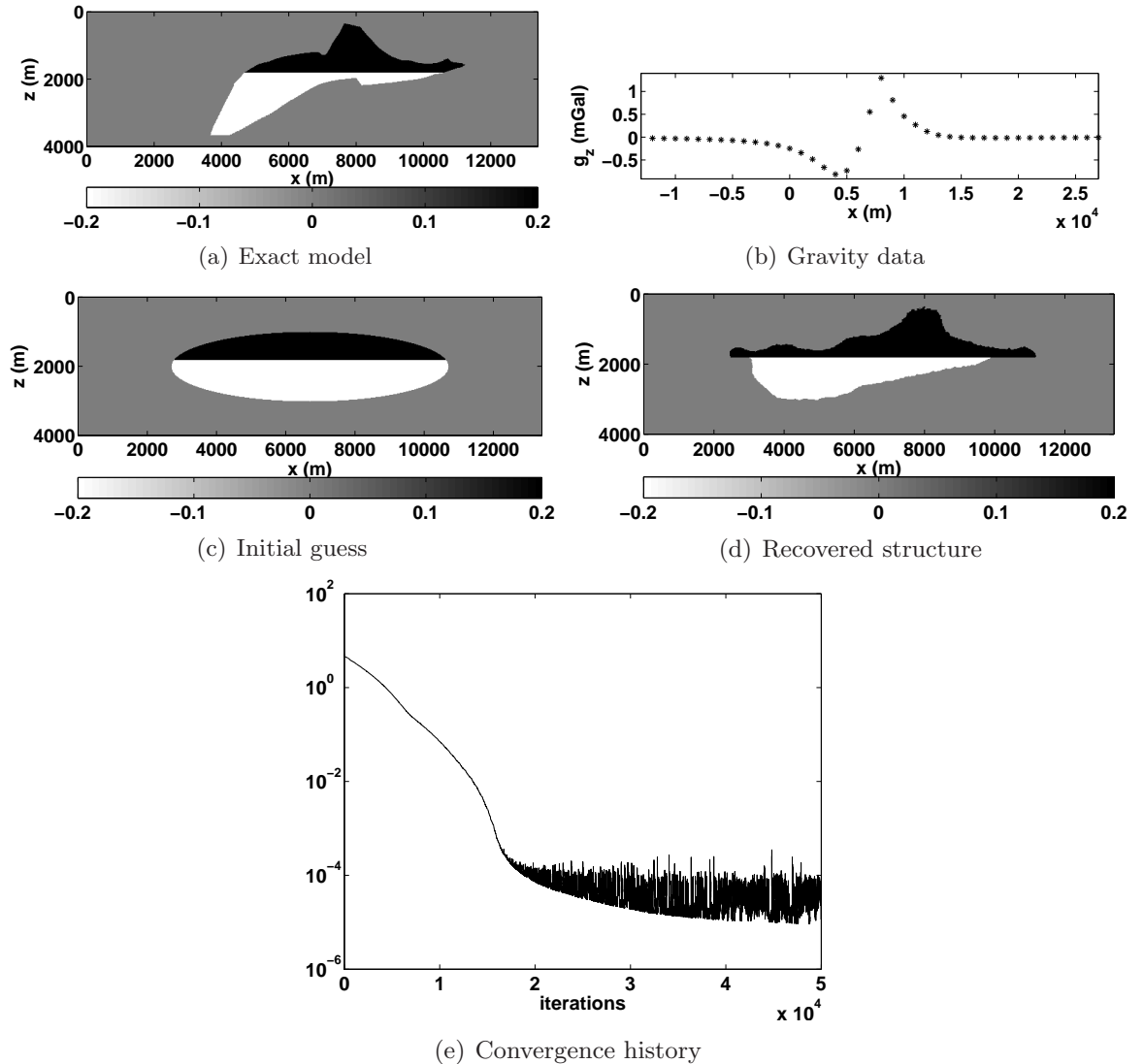


Figure 3: A 2-D slice of the SEG/EAGE salt model with piecewise-constant density contrast. (a) Exact model; (b) Gravity data; (c) Initial guess for the inversion algorithm; (d) Solution after 50000 iterations; (e) Misfit function versus iteration number.

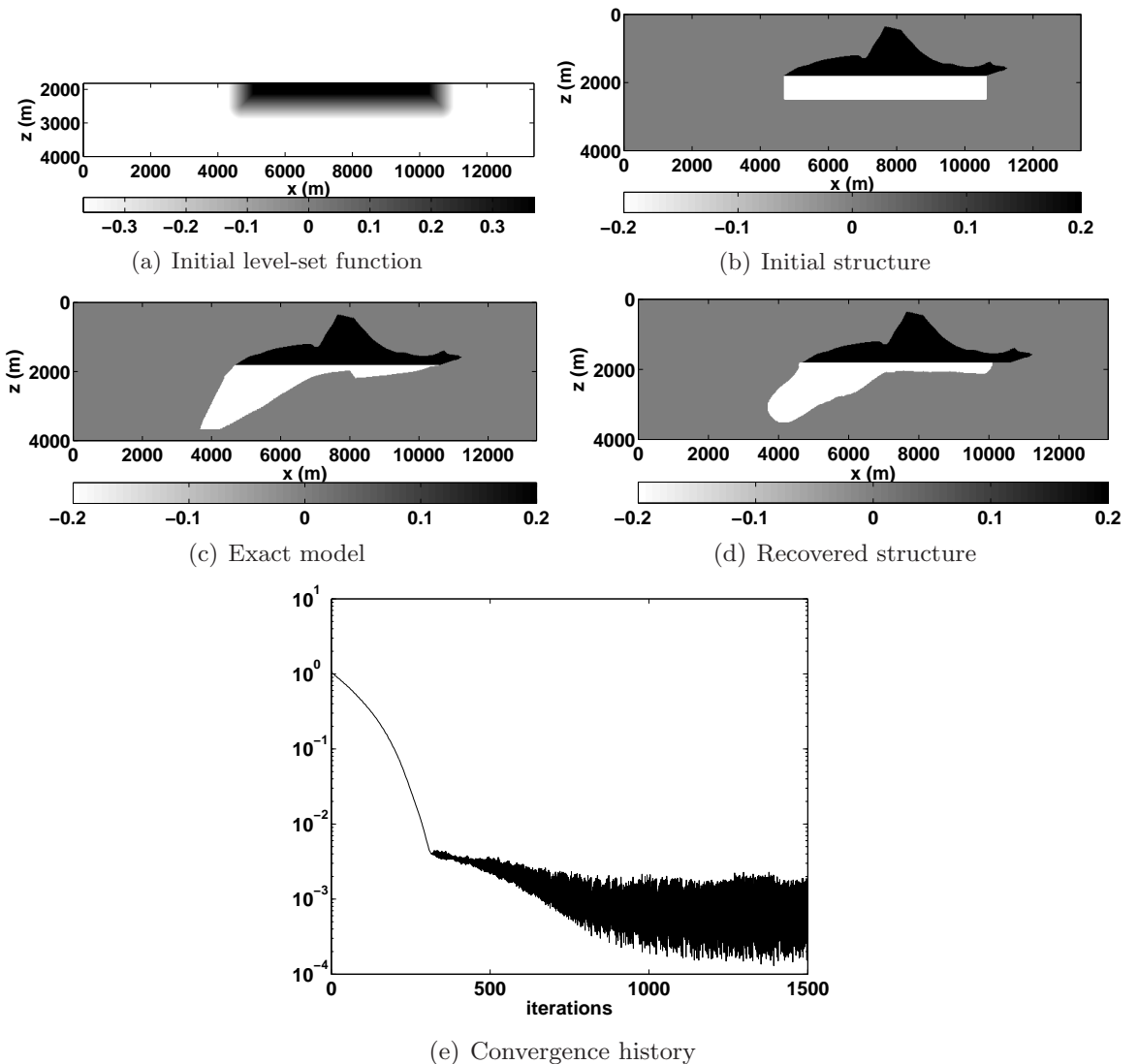


Figure 4: A 2-D slice with a piecewise-constant density contrast; the top of the salt body is constrained and the computation is performed in the sub-domain  $\{z > 1800\text{ m}\}$ . (a) Initial guess of the level-set function; (b) Initial structure in the full domain; (c) Exact model; (d) Recovered solution after 1500 iterations; (e) Misfit function versus iteration number.

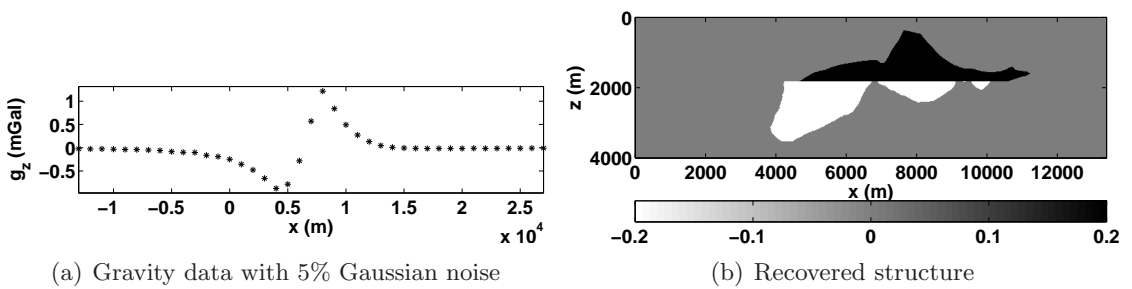


Figure 5: A 2-D slice with a piecewise-constant density contrast; 5% Gaussian noise is added to the measurement. The top of the salt body is constrained and the computation is performed in the sub-domain  $\{z > 1800 \text{ m}\}$ . (a) Gravity data with 5% Gaussian noise; (b) Solution after 1500 iterations.

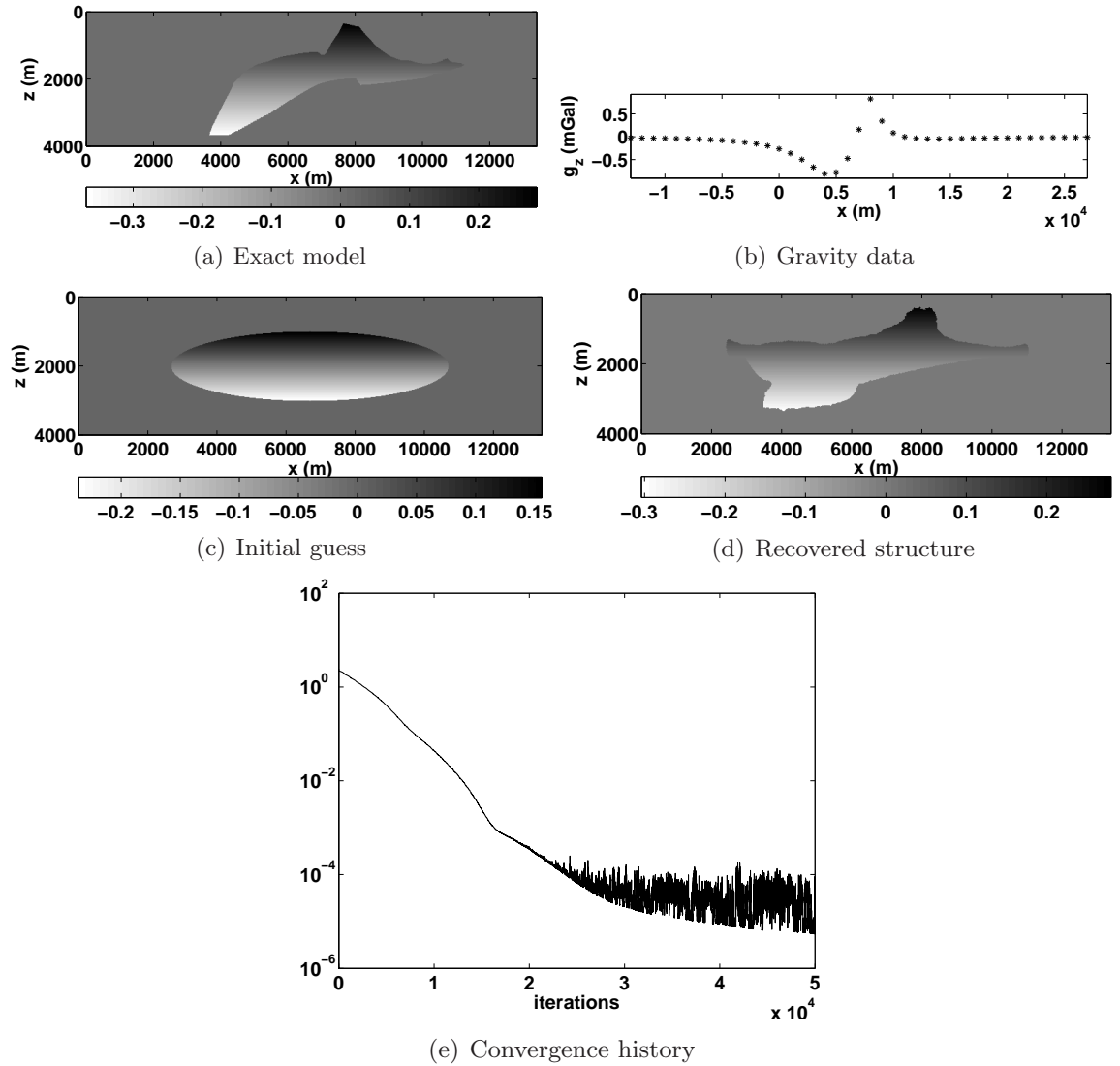


Figure 6: A 2-D slice of the SEG/EAGE salt model with a linearly decreasing density contrast. (a) Exact model; (b) Gravity data; (c) Initial guess for the inversion algorithm; (d) Solution after 50000 iterations; (e) Misfit function versus iteration number.

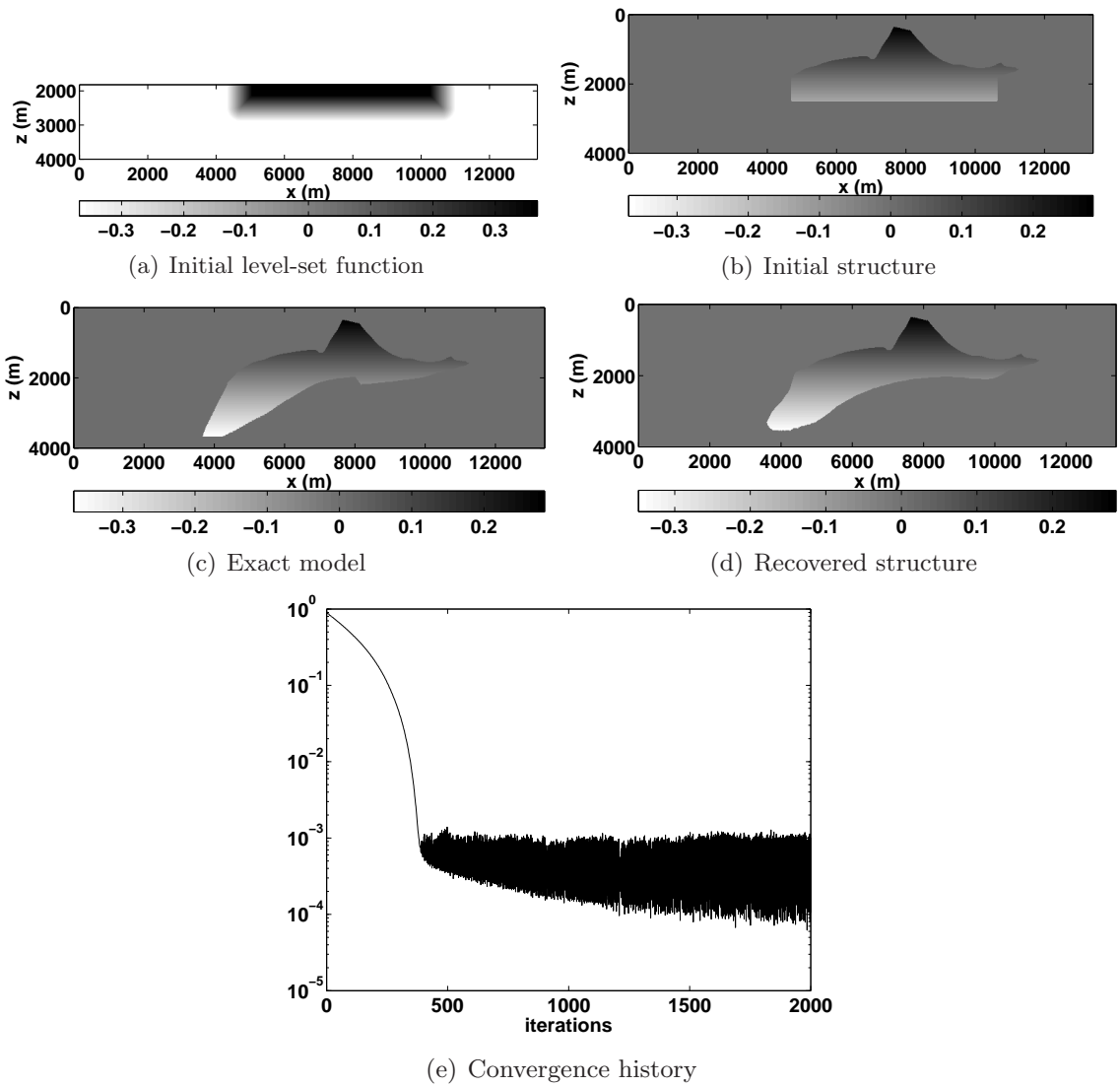


Figure 7: A 2-D slice with a linearly decreasing density contrast; the top of the salt body is constrained and the computation is performed in the sub-domain  $\{z > 1800 \text{ m}\}$ . (a) Initial guess of the level-set function; (b) Initial structure in the full domain; (c) Exact model; (d) Recovered solution after 2000 iterations; (e) Misfit function versus iteration number.

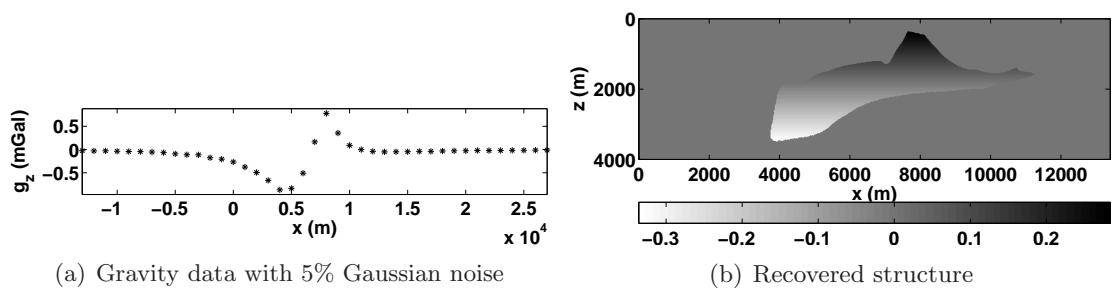


Figure 8: A 2-D slice with a linearly decreasing density contrast; 5% Gaussian noise is added to the measurement. The top of the salt body is constrained and the computation is performed in the sub-domain  $\{z > 1800 \text{ m}\}$ .

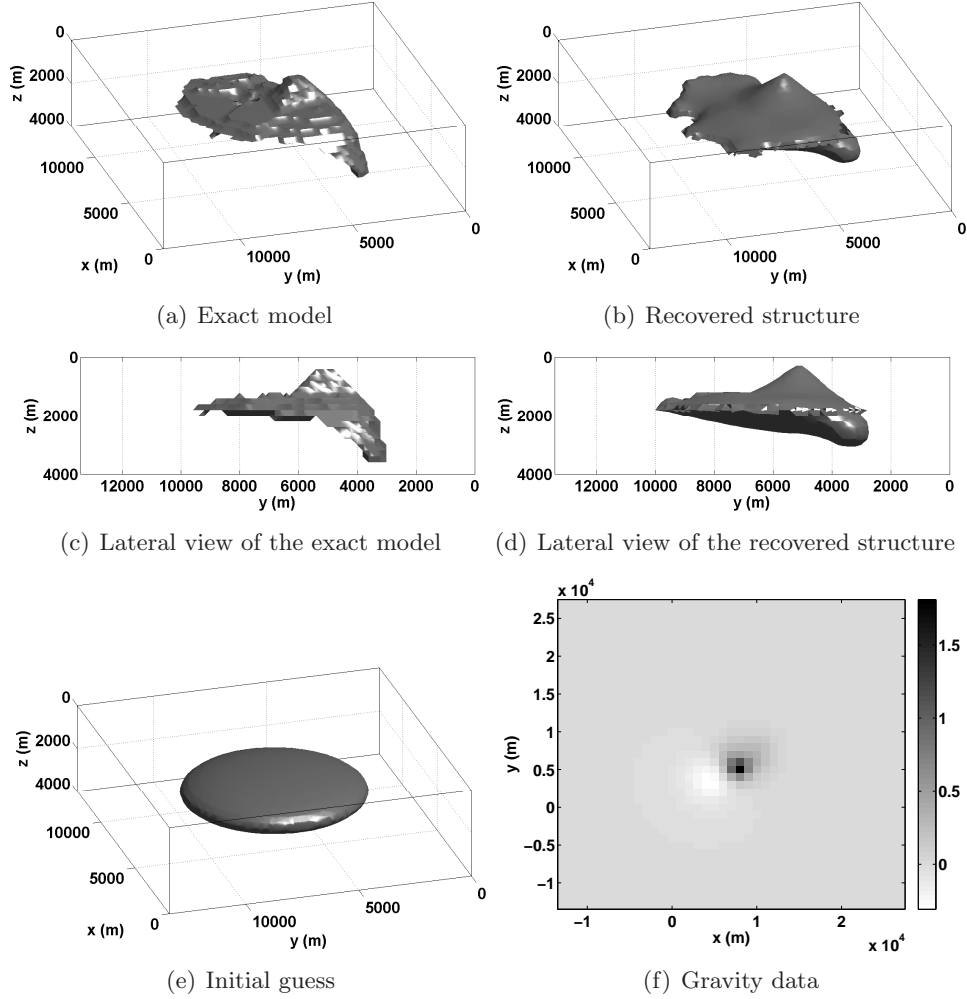


Figure 9: A 3-D SEG/EAGE salt model. (a) Exact model; (b) Solution after 8000 iterations; (c) Lateral view of the exact model; (d) Lateral view of the solution; (e) Initial guess for the inversion algorithm; (f) Gravity data.

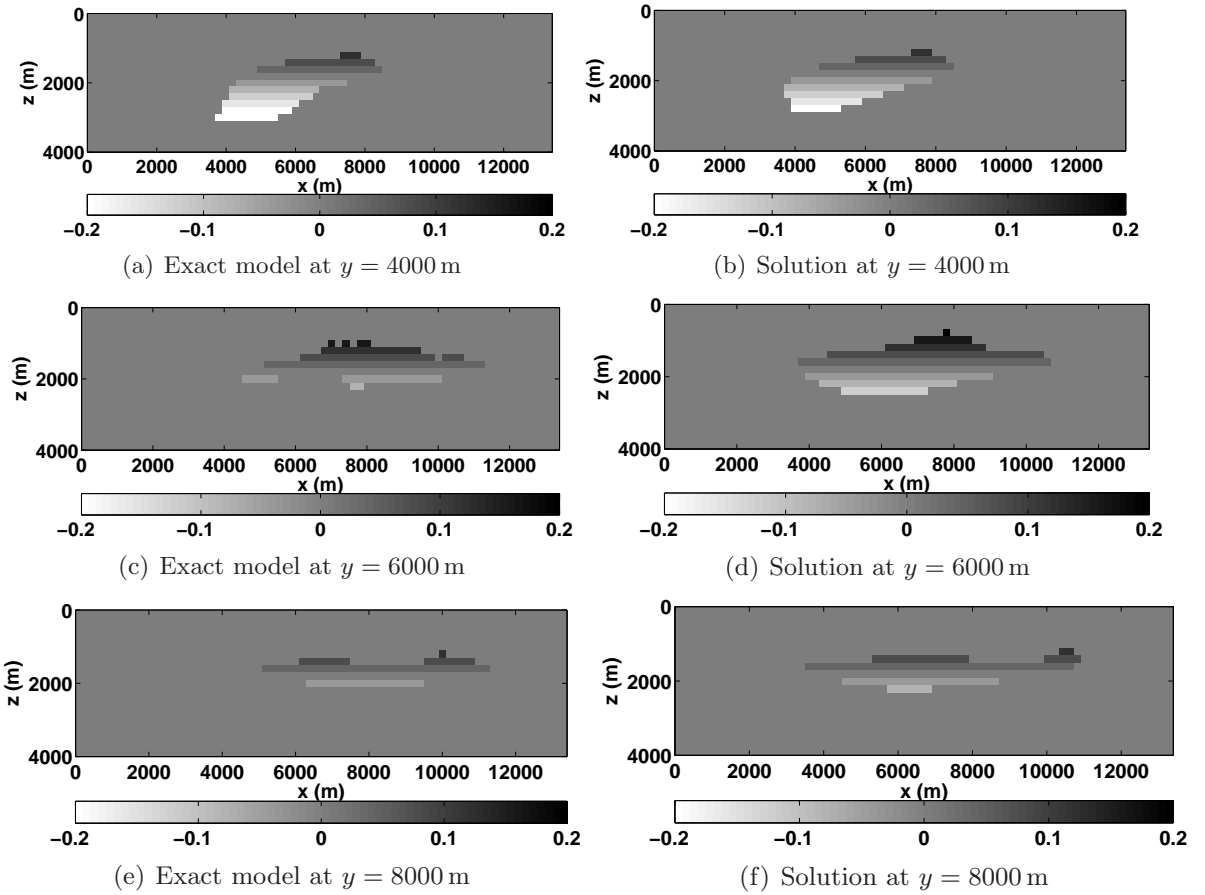


Figure 10: A 3-D SEG/EAGE salt model. Cross-sections at  $y = 4000$  m,  $y = 6000$  m and  $y = 8000$  m of the exact and recovered model.

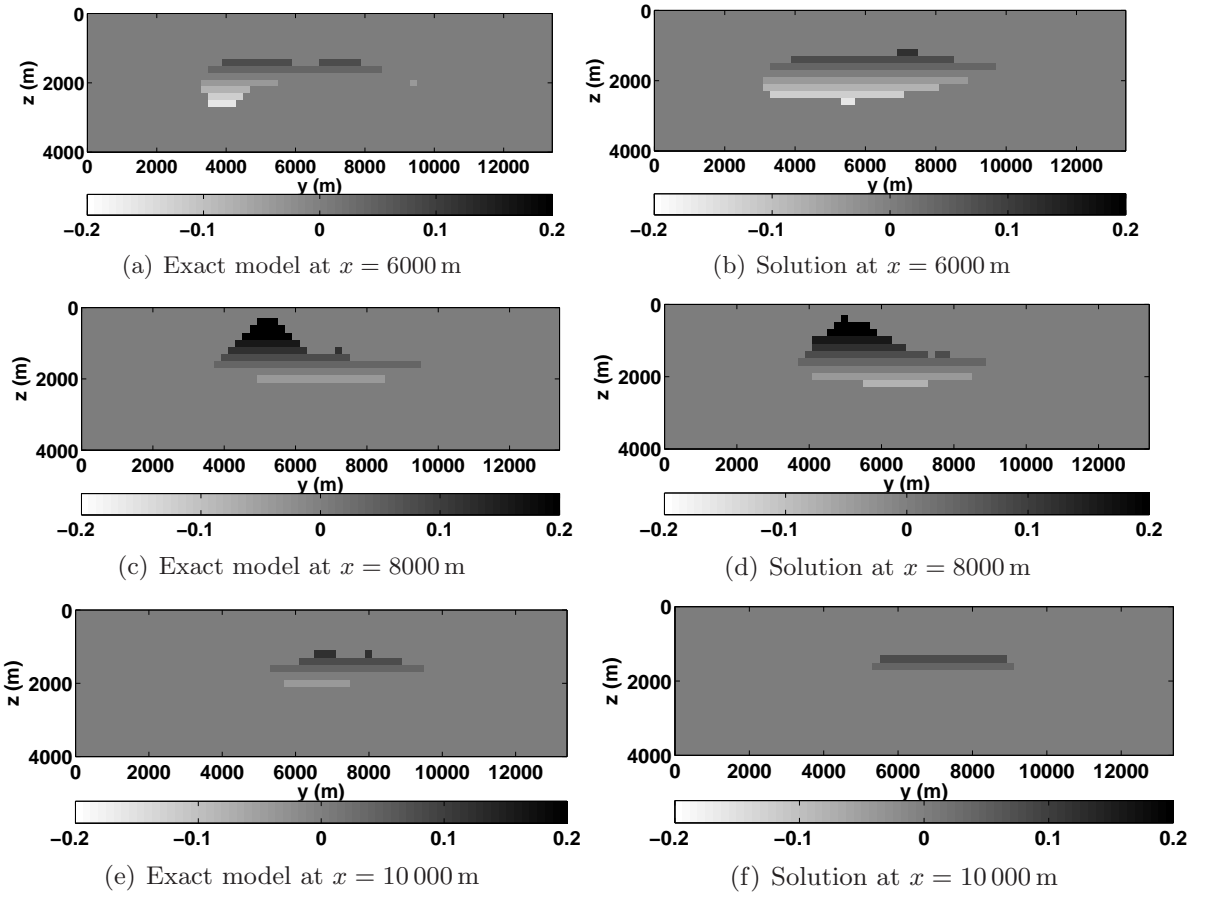


Figure 11: A 3-D SEG/EAGE salt model. Cross-sections at  $x = 6000$  m,  $x = 8000$  m and  $x = 10000$  m of the exact and recovered model.

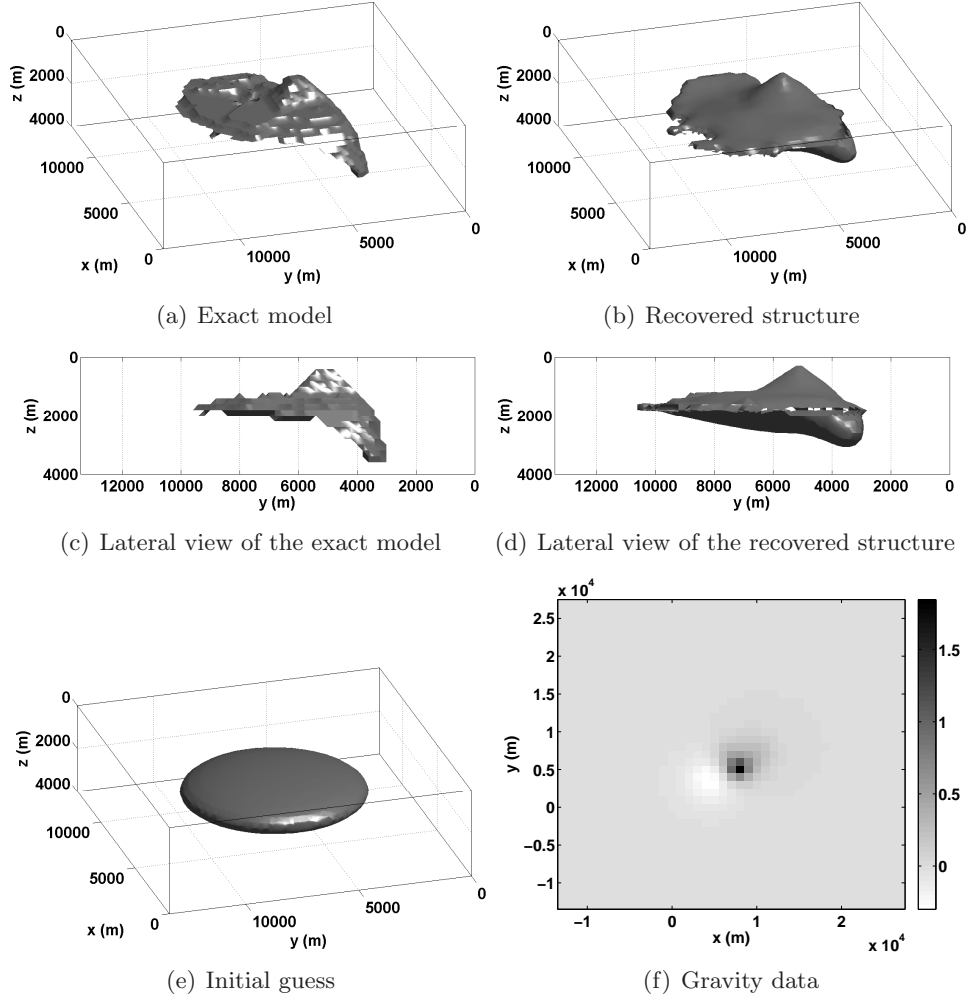


Figure 12: A 3-D SEG/EAGE salt model with 2% Gaussian noise added to the measurement. (a) Exact model; (b) Solution after 8000 iterations; (c) Lateral view of the exact model; (d) Lateral view of the solution; (e) Initial guess for the inversion algorithm; (f) Gravity data.

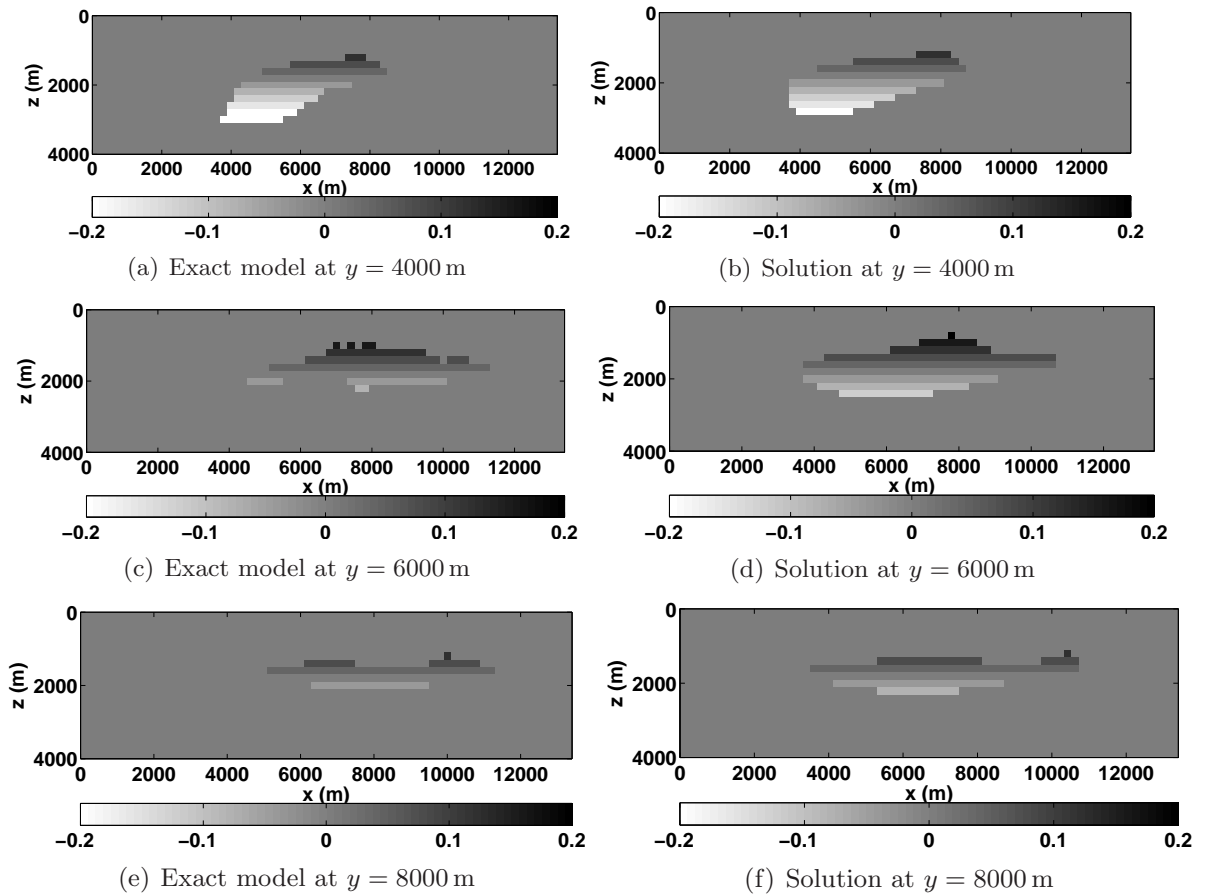


Figure 13: A 3-D SEG/EAGE salt model with 2% Gaussian noise added to the measurement. Cross-sections at  $y = 4000$  m,  $y = 6000$  m and  $y = 8000$  m of the exact and recovered model.

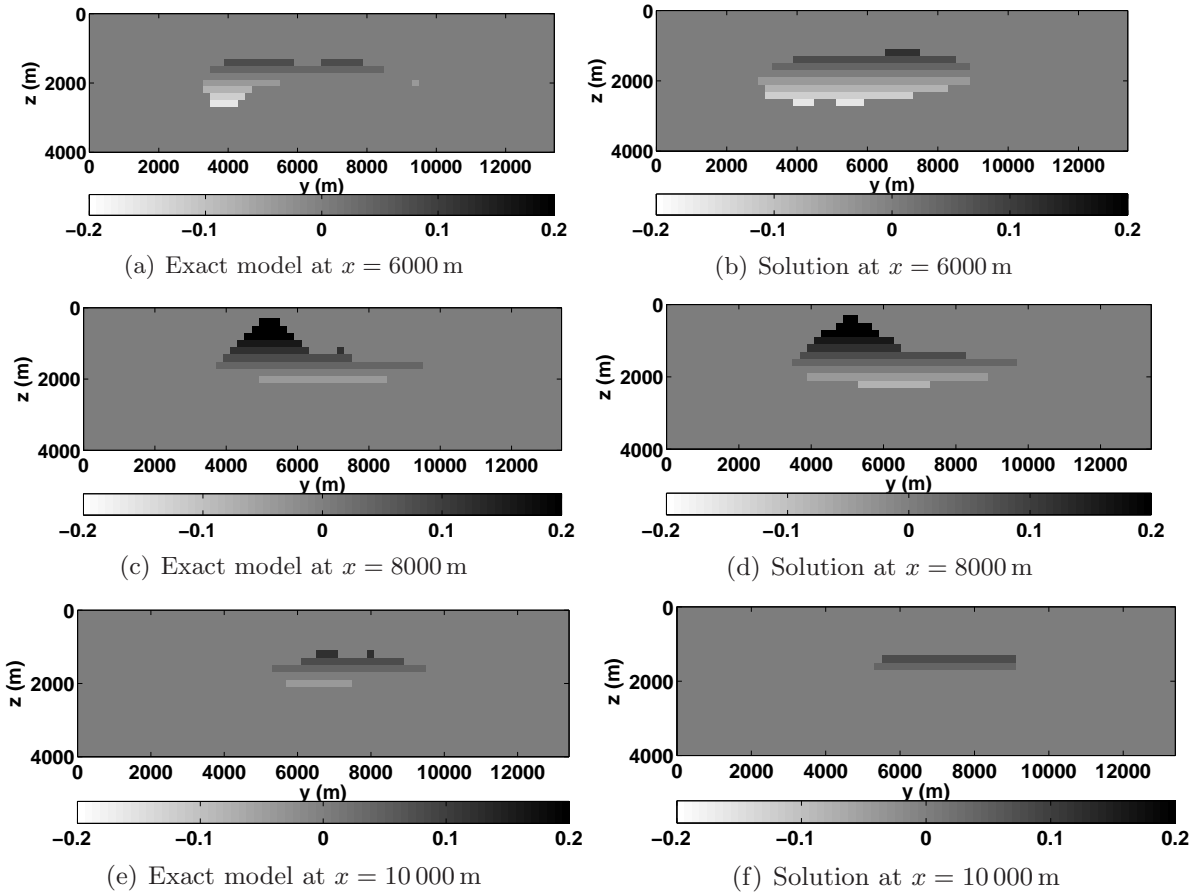


Figure 14: A 3-D SEG/EAGE salt model with 2% Gaussian noise added to the measurement. Cross-sections at  $x = 6000$  m,  $x = 8000$  m, and  $x = 10\,000$  m of the exact and recovered model.

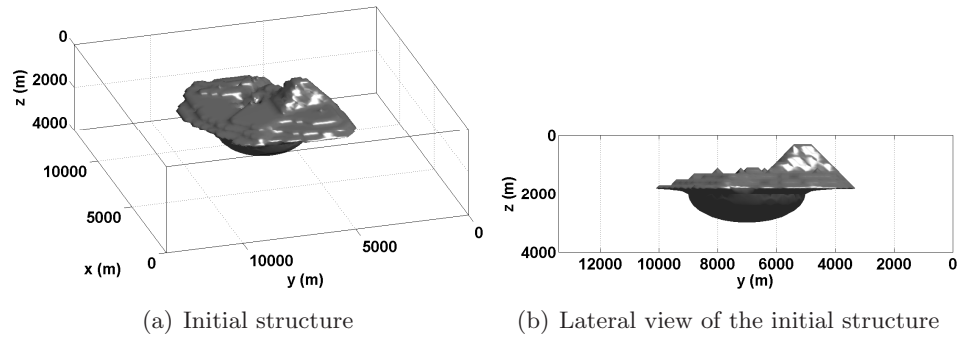


Figure 15: A 3-D SEG/EAGE salt model; the top of the salt body is constrained and the computation is performed in the sub-domain  $\{z > 1800 \text{ m}\}$ . Display of the initial guess.

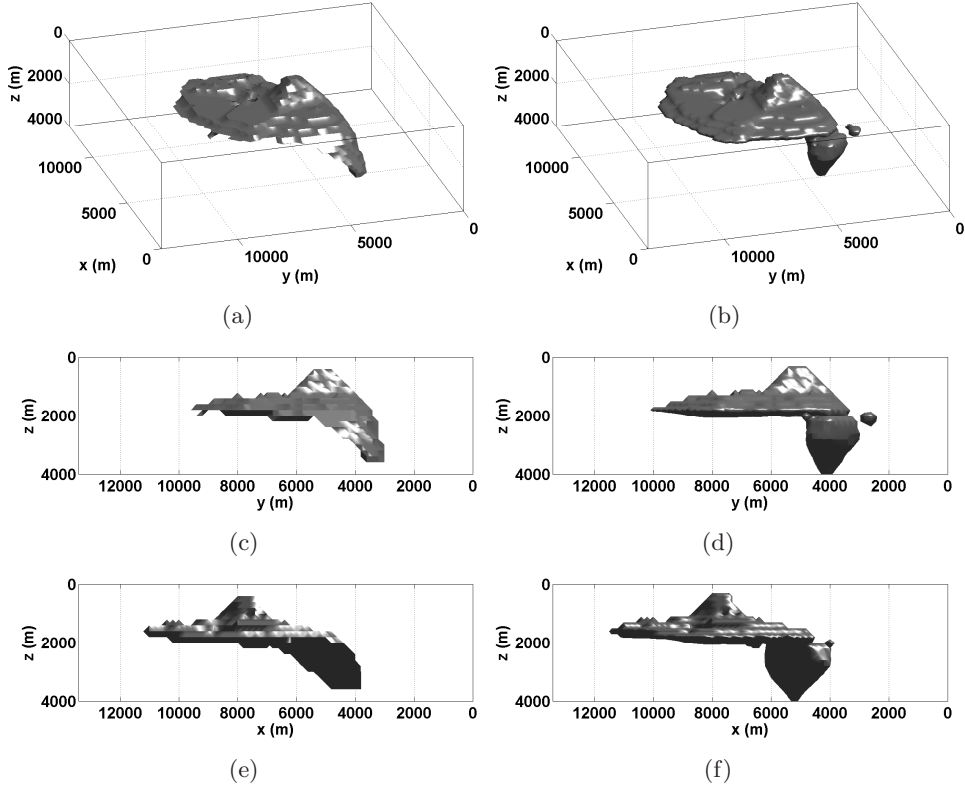


Figure 16: A 3-D SEG/EAGE salt model; the top of the salt body is constrained and the computation is performed in the sub-domain  $\{z > 1800 \text{ m}\}$ . (a) The exact structure; (b) The recovered solution; (c) Lateral view of the exact structure along the  $x$ -axis; (d) Lateral view of the recovered solution along the  $x$ -axis; (e) Lateral view of the exact structure along the  $y$ -axis; (f) Lateral view of the recovered solution along the  $y$ -axis.

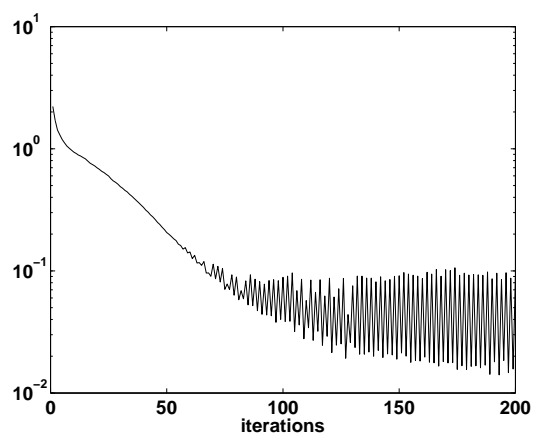


Figure 17: A 3-D SEG/EAGE salt model; the top of the salt body is constrained and the computation is performed in the sub-domain  $\{z > 1800 \text{ m}\}$ . History of convergence.

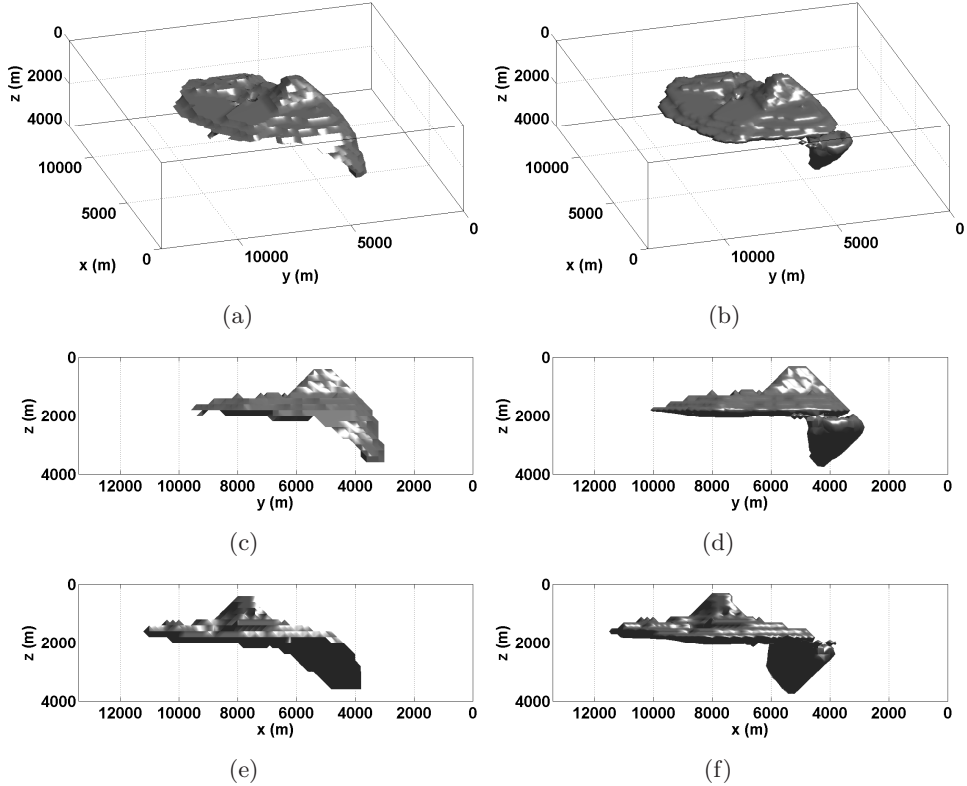


Figure 18: A 3-D SEG/EAGE salt model with 2% Gaussian noise added to the measurement; the top of the salt body is constrained and the computation is performed in the sub-domain  $\{z > 1800 \text{ m}\}$ . (a) The exact structure; (b) The recovered solution; (c) Lateral view of the exact structure along the  $x$ -axis; (d) Lateral view of the recovered solution along the  $x$ -axis; (e) Lateral view of the exact structure along the  $y$ -axis; (f) Lateral view of the recovered solution along the  $y$ -axis.

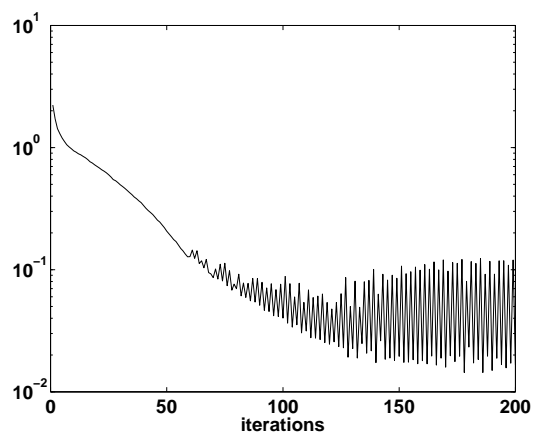


Figure 19: A 3-D SEG/EAGE salt model with 2% Gaussian noise added to the measurement; the top of the salt body is constrained. History of convergence.